ADVANCED MATERIALS
www.advmat.de

Mechanically Reinforced Skin-Electronics with Networked Nanocomposite Elastomer

Seungyong Han, Min Ku Kim, Bo Wang, Dae Seung Wie, Shuodao Wang, and Chi Hwan Lee**

Rapid development of mechanically non-conventional electronics opens up a new prospect in the field of skin-mountable electronics that can intimately contact to the skin while maintaining functionality and integration under repeated deformations such as bending, stretching, compressing, and twisting.[1–9] Examples range from sensors for monitoring temperature, pressure, oxygen concentration of blood, and electrophysiological activities to actuators for providing therapeutic heat and healing factors.[10–14] Coplanar thin films formed with ductile metals such as gold (Au), copper (Cu), silver (Ag), and platinum (Pt) serve as the conductive electrodes in the devices while precisely engineered stretchable layouts such as filamentary serpentines, self-similar fractals, and horseshoes simultaneously allow efficient accommodation of mechanical deformations.[15–19] A key challenge still remains in the potential for catastrophic failures of such electrodes that might happen by unpredictable consequences such as inadvertent over-stretching beyond the fracture limits, defect-driven cracks, and edge-initiated delamination. Recent advances could alleviate the issues by exploiting microfluidic structures where the ultralow modulus materials embedded inside a microfluidic space can efficiently isolate the mechanics associated with the constituent thin film-based electrodes from the supporting elastomeric substrate/encapsulate.[20,21] These strategies provide valuable means to endow the systems with necessary mechanical properties although they require additional layers for the packaging matrix, leading to increased volume of entire structure.

Here, we introduce a simple, straightforward strategy by exploiting nanocomposite elastomers that combine with highly networked 1D metallic nanowires (NWs) to serve as functional electrodes in skin-mountable electronic devices. The strategy provides a route to enhance important mechanical properties of the ultrathin, conformable electronics against fracture and delamination phenomena, which would be beneficial to the extension of service lifetime. Theoretical and experimental studies reveal that this type of highly networked nanocomposite elastomers exhibit superior crack resistance, contact adhesion, and normal/shear strength in comparison to the conventional thin film-based counterparts. Device demonstrations in thermotherapeutic treatments for the joint, surface temperature mapping over the skin, and electrophysiological monitoring from the heart and the muscle illuminate the potential for practical applications with importance in human healthcare.

A nanocomposite elastomer contains a layer of highly networked NWs and diluted polyimide (D-PI, 1:1 ratio mixture of polyimide and 1-methyl-2-pyrrolidinone) to serve as electrical conducting components and elastomeric substrate matrices, respectively. Herein, Cu NWs or Ag NWs are studied due to their high electrical conductivity as well as excellent elongation.[22–24] More information associated with the use of nanowires in conducting electrodes appears in previous reports.[25–28] **Figure 1**a shows optical images of the as-prepared Cu NWs on a temporary supporting substrate. The synthesis with the solution-based nucleation-and-growth mechanism allows the growth of Cu NWs up to ≈50 μm in the maximum length, easily leading to a networked mesh form. Details about the synthesis appear in the Experimental Section. Results of the X-ray diffraction (XRD; normal powder X-ray diffractometer; RIGAKU, D/MAX-2500, ≈40 kV, ≈300 mA) analysis in Figure 1b indicate the crystallographic structure of the Cu NW mesh where the diffraction peaks imply the cubic form of metallic Cu (ICDD, No. 00-004-0836). The optical images and XRD analysis for as-prepared Ag NWs (maximum length: ≈250 μm) appear in Figure S1 (Supporting Information).

Figure 1c presents a schematic illustration for the construction procedures of a device architecture. The fabrication begins with a temporary supporting Si wafer by stacking thin films of nickel (Ni, 300 nm thick), D-PI (300 nm thick), and NW mesh (600 nm thick). Photolithographic patterning and dry etching define the layouts of the NW mesh in a stretchable form such as filamentary serpentine traces. The stacked structure (Si wafer/Ni/D-PI/NW mesh) is then immersed in deionized water at

Dr. S. Han
Department of Materials Science and Engineering
Frederick Seitz Materials Research Laboratory
University of Illinois at Urbana-Champaign
Urbana, IL 61801, USA
M. K. Kim, D. S. Wie
School of Mechanical Engineering
Purdue University
West Lafayette, IN 47907, USA
Dr. B. Wang, Prof. S. Wang
School of Mechanical and Aerospace Engineering
Oklahoma State University
Stillwater, OK 74078, USA
E-mail: shuodao.wang@okstate.edu
Prof. C. H. Lee
Weldon School of Biomedical Engineering
School of Mechanical Engineering
Center for Implantable Devices
Birck Nanotechnology Center
Purdue University
West Lafayette, IN 47907, USA
E-mail: lee2270@purdue.edu

DOI: 10.1002/adma.201603878

ADVANCED MATERIALS
www.advmat.de

www.MaterialsViews.com

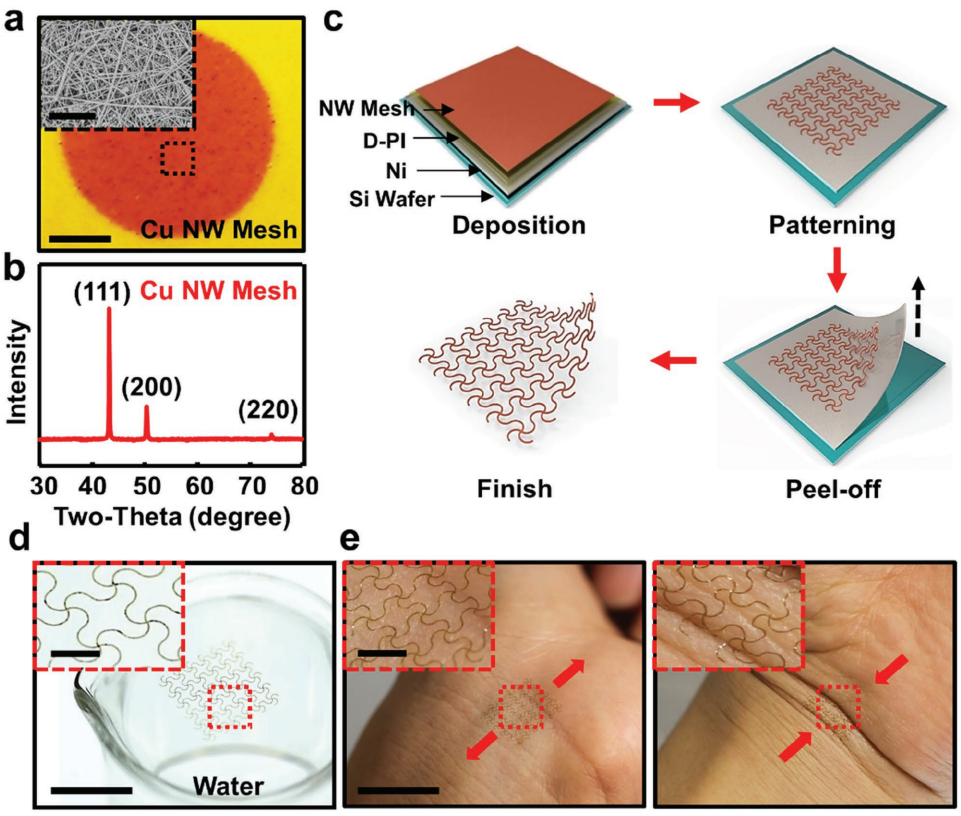

Figure 1. Materials for a networked nanocomposite elastomer and a device architecture in a design with stretchable layouts. a) Optical image and scanning electron microscopy (SEM) image of as-prepared Cu NWs that form a highly networked mesh structure on a temporary supporting substrate. All scale bars are 1 cm and 10 µm (inset). b) Results of X-ray diffraction (XRD) for the as-prepared Cu NW mesh. c) Schematic illustration of the key steps in the construction of a device architecture. d) Optical image of the completed device architecture afloat on the surface of water. Enlarged inset image highlights a single filamentary serpentine unit. All scale bars are 1 cm and 1.5 mm (inset). e) Optical images of the device architecture integrated onto the skin of wrist under complete stretching (left) and compressing (right). Enlarged inset images highlight the highly intimate contacts onto the skin maintained during the mechanical deformations. All scale bars are 1 cm and 2 mm (inset).

room temperature, followed by a mechanical peeling of the layers (Ni/D-PI/NW mesh) from the Si wafer. Here, the ductile Ni film serves as a strain inducer that can mechanically deform molecular bonding at the interface, thereby inducing electrostatic charges to attract water molecules. Subsequent chemical reactions facilitate the mechanical debonding at significantly decreased peeling energy, enabling intact delamination of the stacked layers from the Si wafer. The basic mechanism of this process relies on the water-assisted subcritical debonding phenomenon.[29–31] The Ni layer on the bottom of the delaminated structure is then removed by immersing in iron chloride ($FeCl_3$) for ≈30 s. Details about the construction procedures appear in the Experimental Section. Figure 1d shows a completed testbed structure afloat on the surface of water relying on the surface tension (Figure S2, Supporting Information), facilitating easy transfer onto the skin. Figure 1e presents that the transferred structure onto the wrist while maintaining high level of conformal contacts onto the skin under complete stretch (left image) and contraction (right image) without any adhesive agent (e.g., spray-on-bandage), used in previous reports.[32] When detached from the skin, the ultrathin structure collapses on itself due to the ultra-deformability, as also observed in traditional ultrathin skin-electronics.[3] Reusable skin-electronics exist in a relatively thicker (>≈100 µm thick) form by exploiting encapsulation packages consisting of various soft materials.[21,33,34]

The materials and design layouts allow to minimize the induced strain occurring during large deformations under stretching. **Figure 2**a shows a series of optical images of a testbed structure under stepwise tensile strain (ε) at 0%, 55%, and 80%. The results show that the structure can be stretched up to ≈80% without any evidence of plastic deformations or fractures, likely due to the excellent mechanical strength and elongation capacity of the embedded NWs.[22] The large stretchability becomes more important especially when the device serves as a monitoring system in an array type for large areas. In comparison, a bare elastomer (without the embedded NWs) patterned into the same geometry exhibits non-recoverable plastic deformations when stretched by more than 55% (Figure S3, Supporting Information). These experimental results agree well with the finite element analysis (FEA, see the Experimental Section for details), as shown in Figure 2b, confirming that the maximum principle strains in the single trace unit are still below the fracture limit of the networked Cu NWs (≈30%, further discussed in the end of this section) up to at ≈80% stretch

DOI: 10.1002/adma.201603878

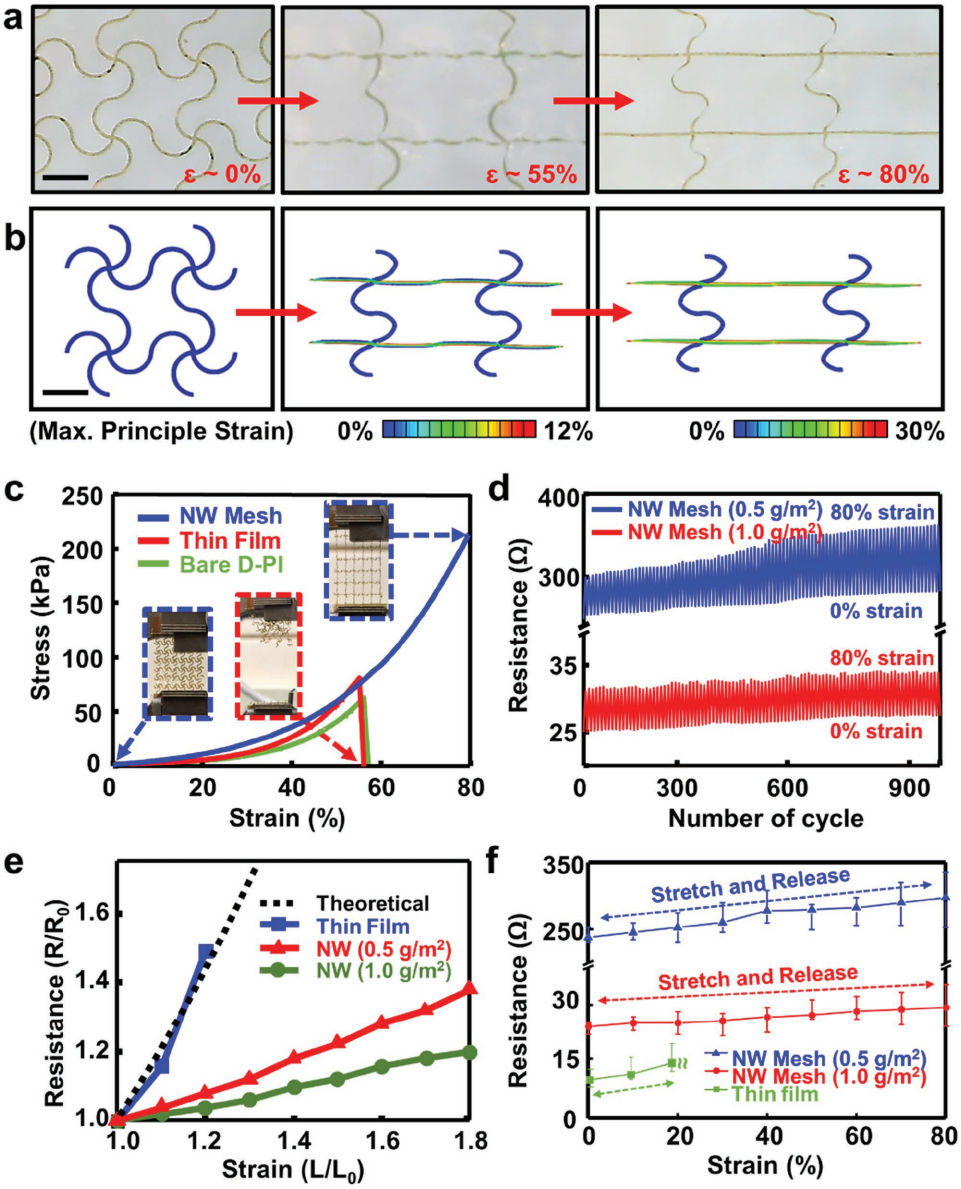

Figure 2. Mechanical properties of networked nanocomposite elastomers under stretching. a) Optical images of a networked nanocomposite elastomer embedded with Cu NW mesh at different tensile strains at 0% (left frame), 55% (middle frame), and 80% (right frame). Scale bar is 500 μm. b) Results of finite element analysis (FEA) for the maximum principle strain in the traces under the stretching. c) Experimental results for stress–strain response of this type of a nanocomposite elastomer (blue line) in comparison to a thin film-based elastomer (red line) and a bare elastomer (green line). d) Change of resistance in the elastomers with varied density of Cu NWs under stretching at ≈80% over 1000 repetitive cycles. e) Normalized resistance–strain curves for the elastomers in comparison to a thin film-based elastomer. Black dotted line denotes a theoretical curve, $R/R_0 = (L/L_0)^2$. f) Corresponding absolute resistance–strain curves for all the elastomers.

(Figure 2b, right), while a traditional Cu thin film-embedded structure fractures at ≈55% stretch (Figure 2b, middle) when the local strain exceeds the fracture limit (≈12%).[35] For comparison, the extensive analysis of similar serpentine layouts with Cu thin films appears in previous studies.[3,36,37] Figure 2c shows representative experimental results of stress–strain curves, obtained from a dynamic mechanical analyzer (DMA, TA Instruments, Q800, ≈10 kPa min^{-1}) for a Cu NW mesh-embedded elastomer (blue line), a Cu thin film-embedded elastomer (red line), and a bare elastomer (green line). The results show that the maximum strains (before fracture) of the NW mesh-embedded elastomer are ≈20% higher than those of the thin film-embedded elastomer and bare elastomer while the effective tensile moduli are similar (≈200 kPa) for all the cases. Figure 2d confirms that the electrical connections in the NW mesh maintain at $\varepsilon \approx 80\%$ over ≈1000 repetitive cycles without significant degradations. The resistance of the low density specimen (≈0.5 g m^{-2}, blue line) slightly increases after ≈500 loading cycles whereas the high density specimen (≈1.0 g m^{-2}, red line) retains the consistent

resistance at ≈30 Ω during the entire cycles, implying that more networked NWs can reduce the possibility to disconnect the conducting paths.

The advantages of the highly networked NWs include the enhancement of crack resistance due to the randomly oriented junctions of NWs that allow suppressing the initiation and propagation of cracks.[38] Figure 2e shows representative experimental resistance–strain curves for the Cu NW mesh-embedded elastomer (≈1.0 and ≈0.5 g m^{-2} for the green and red lines, respectively) and a control Cu thin film-embedded elastomer (blue line) along with the theoretical curve (black dotted line), $R/R_0 = (L/L_0)^2$, where R/R_0 and L/L_0 are normalized resistance and length, respectively. The theoretical curve defines the relation between R/R_0 and L/L_0 for the polymer-supported metal thin films when no crack occurs under stretching where any deviation above this curve implies possible crack formations.[39–41] The results show that the normalized electrical resistances of the thin film-based elastomer (blue line) are close to the theoretical values and ≈25 times higher than those of the nanocomposite elastomers (red and green lines) at $\varepsilon \approx 20\%$. This efficacy is more obvious in the higher density specimen, implying that denser networked NWs resist more efficiently against crack. The denser networked NWs exhibit less change of resistance under the stretching due to the plentiful existence of NW junctions that serve as electrical paths, whereas the sparsely networked NWs are more susceptible to the strain.[41–44] Figure 2f presents the absolute resistances during the cyclic elongations under repetitive stretching and releasing, highlighting that the resistances of the Cu NW mesh-embedded elastomers almost recover upon releasing of the applied strains up to ≈80%. The corresponding experimental results by exploiting Ag NWs are summarized in Figure S4 (Supporting Information), which are consistent with those obtained with Cu NWs.

The mechanism of the well-maintained electrical conductions in the NW mesh-embedded elastomers involves the characteristic deformations of the networked NWs under stretching. For instance, at low strains, the networked NWs change their shapes by aligning themselves to the applied strain direction, and thereby efficiently accommodating the mechanical deformations without significant degradations in the conduction paths. Beyond the failure limits ($\varepsilon > 80\%$), the networked NWs begin to partly rupture rather than the catastrophic cracking (as typically observed in the thin films), and thereby the intact NWs can still serve as a conducting electrode (Figure S5, Supporting Information). The FEA studies as shown in Figure S6 (Supporting Information) reveal the underlying mechanism of this advantage. When stretched, the randomly oriented Cu NWs slide against each other and rotate to the stretching direction. This extra degree of freedom in the NWs allows to release the strain energy and prevent singular deformations at the junctions. Therefore, although each single Cu NW has the fracture limit of 3.0% which is much smaller than that of Cu thin film (≈12%),[45] the networked NWs can sustain up to ≈30% of local strain before fracture. Details about the simulation appear in the Experimental Section. It is noteworthy that such sliding of NWs by the applied strains can shift the contact junctions between NWs, causing the electrical resistance to change.[46] The serpentine layout incorporated in the networked NWs can suppress the sliding events by distributing the strains in a wider region of deformed meanders instead of being concentrated in a small region. This presents an important consequence that allows the various devices reported here to be less sensitive to the motion-induced strains by wearers.

The mechanical strength in normal and shear directions is particularly important for various skin-electronics where excessive normal and shear stresses can drive delamination of entire system. **Figure 3**a presents the experimental measurements of normal force obtained from a mechanical T-peeling tester equipped with a high-resolution force gauge (Mark-10, Copiague, NY, resolution: ±0.25%) for a Cu NW mesh (red line, 1.0 g m^{-2}) and a control Cu thin film (blue dotted line, ≈600 nm thick) integrated onto an artificial synthetic skin (Ecoflex, $E \approx 125$ kPa, ≈2 mm thick, modulated with human skin-like textures). Details about the fabrication procedures and optical images of the artificial synthetic skin appear in the Experimental Section and Figure S7 (Supporting Information), respectively. A strong adhesive electrical insulation tape (Tapes Master, KP-1M-36-12) allows initiating the peeling at a constant rate of 1 mm min^{-1} with 90° to the surface (Figure S8, Supporting Information). The results clearly show that the initial peak peeling force near the edges for the NW mesh-embedded elastomer (≈1.4 N) is almost threefold higher than that of the thin film-based elastomer (≈0.5 N), most likely due to the significantly increased surface contact areas of the NW mesh. The experimental measurements of the surface topography obtained from an atomic force microscopy (AFM, Asylum Research, MFP-3D) appear in Figure S9 (Supporting Information), presenting that the surface areas of the Cu NW mesh are >≈1000 times higher than those of the Cu thin film. The enhanced initial peak peeling force is highly desirable for any skin-mountable systems because the propensity for delamination exists mostly at/near edges due to the concentrated stresses. Figure 3b shows an optical image (left) and a scanning electron microscope (SEM) image (right) of the NW mesh-embedded elastomer adhered onto the surface of the artificial skin seamlessly with high level of conformity, which follows most of the topography of the surface by penetrating into the deepest creases and pits.

Figure 3c shows experimental results of shear forces obtained from a nanoindentation tester (Hysitron, TI950 TriboIndentor) by scratching a diamond tip across the surface of a Cu NW mesh (left image, ≈600 nm thick) and a control planar Cu thin film (right image, ≈600 nm thick) integrated onto a supporting artificial skin (Figure S10, Supporting Information). The load–unload function during the tests by applying a normal load of ≈8 mN at a constant scratching speed of 0.25 μm s^{-1} in a 15 μm length appears in Figure S11 (Supporting Information). This experimental setup allows recording the exerted forces and displacements to the surfaces in both normal and shear directions, leading to the qualitative evaluations of tribological properties. The results show that the friction coefficient, defined as the ratio of lateral force (F_L) to normal force (F_N), for the surface of the Cu NW mesh (left graph, red line) experiences minor fluctuations at around 0.45 which is ≈60% higher than that for the surface of the Cu thin film (Figure 3c, left graph). The upward trend happens in the friction coefficient due to

Adv. Mater. 2016,
DOI: 10.1002/adma.201603878

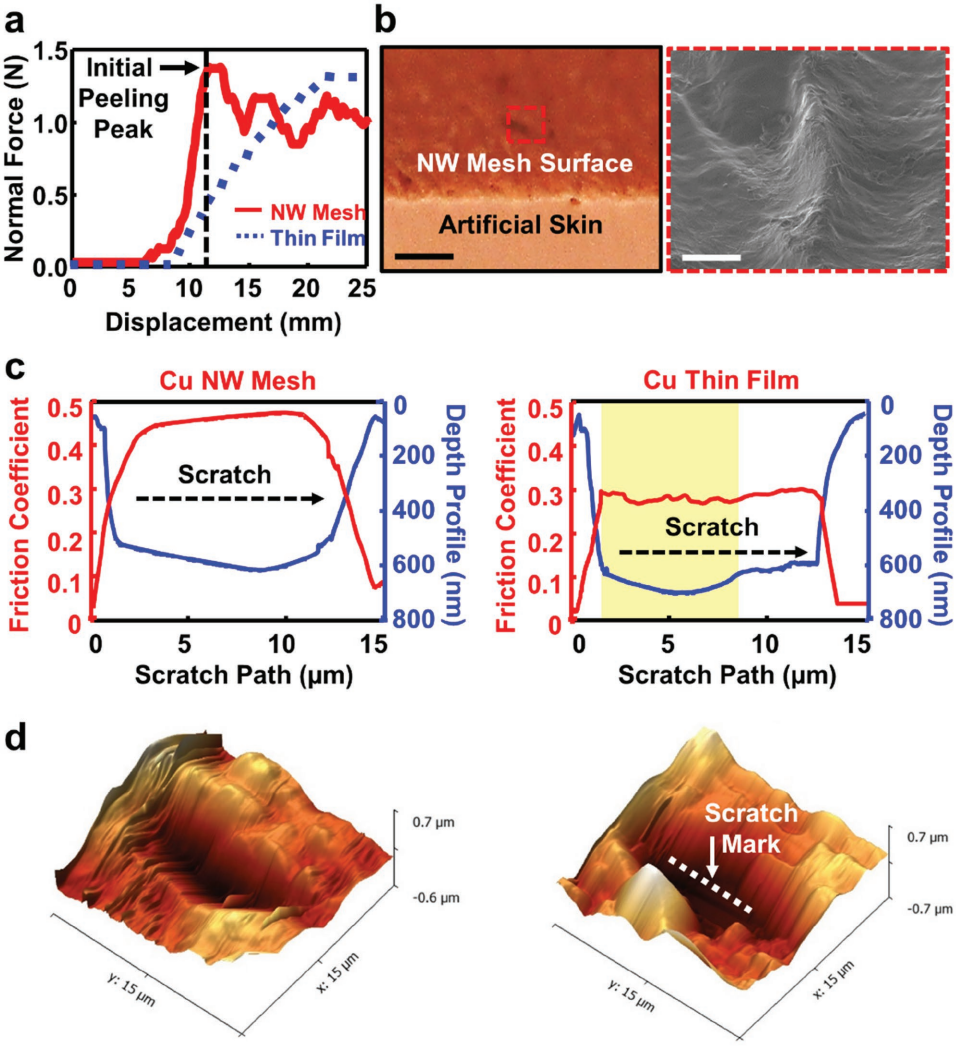

Figure 3. Mechanical strength of networked nanocomposite elastomers in normal and shear directions. a) Results of T-peeling tests for a Cu NW mesh-embedded elastomer (red line) and a Cu thin film-embedded elastomer (blue line) peeled from an artificial skin. b) Optical (left) and SEM (right) image of the Cu NW mesh-embedded elastomer adhered on the artificial skin. All scale bars are 1 mm and 50 μm. c) Results of scratch tests performed on the surface of a Cu NW mesh-embedded elastomer (left) and a Cu thin film-embedded elastomer (right). d) Corresponding atomic force microscopy (AFM) images for the scratched surfaces of the elastomers.

the accumulation of the materials at the scratching tip. On the other hand, remarkable deviations with fluctuations occur in the friction coefficient of the Cu thin film (yellow highlighted area in Figure 3c, right graph, red line), indicating that the properties of the scratched surface are considerably changed. The indentation depth profiles along the scratch path in Figure 3c (blue lines) present that the top surface of the Cu NW mesh is lightly scratched (scratch depth < 600 nm) whereas the Cu thin film is deeply scraped (scratch depth > 600 nm) into the bottom artificial skin. These observations agree well with the surface topographies (Figure 3d) obtained from AFM (Asylum Research, MFP-3D) measurements where the specimen for the Cu thin film exhibits a clear scratch mark left behind on the surface of the artificial skin (highlighted by a white dotted line in Figure 3d, right image).

The mechanical reinforcements of the important characteristics described above provide ideal platforms for applications in broad range of skin-electronics. **Figure 4**a shows a representative example of skin-coupled thermotherapy patch that contains a layer of Cu NW mesh (≈1.0 g m^{-2}, 600 nm thick) and D-PI (300 nm thick) to serve as the Joule-heating element and the supporting layer, respectively. The device takes the form of an engineered open mesh, serpentine layout (inset image) to efficiently accommodate the induced strains under mechanical deformations. Figure 4b shows the temperature distributions, obtained from an infrared (IR) camera (FLIR SC645, sensitivity: 0.05 °C), on the skin of knee heated by a device that follows by delivered powers of 0.08 W (black line), 0.13 W (red line), and 0.23 W (blue line) with an external wire connection. The temperature increases are linearly proportional to the incident power, and therefore can allow the controlled operation of thermotherapy patch. Figure 4c shows experimental demonstrations with activated devices that contain Cu NW mesh-embedded elastomers (0.5 and 1.0 g m^{-2})

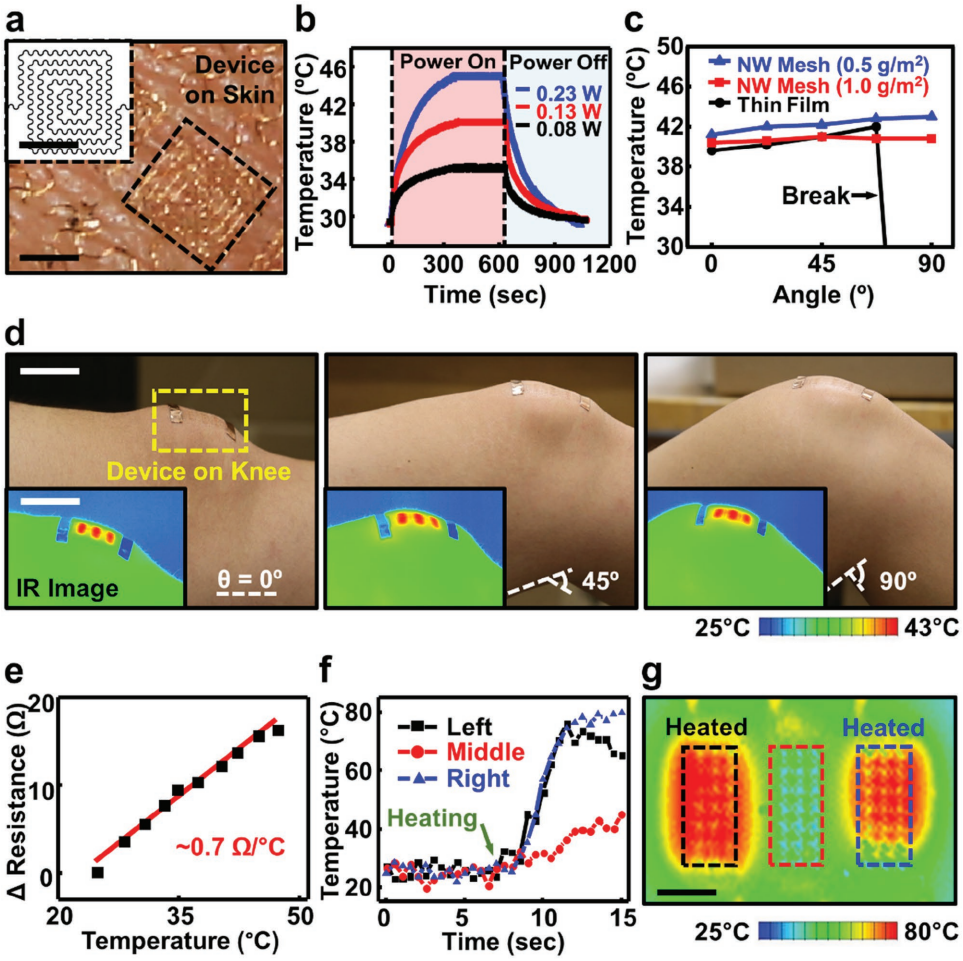

Figure 4. Device demonstrations in a skin-like thermotherapy patch and a 1 × 3 array of temperature sensor. a) Optical image of a representative skin-like thermotherapy patch that contains a layer of Cu NW mesh, all integrated onto the skin of knee. Inset shows an image of the open mesh, serpentine layout. All scale bars are 1 cm. b) Experimental results for the average temperatures of a skin-like patch that follows by varied incident powers from 0.08 to 0.23 W. c) Results of generated heat obtained from the skin-like patches on the knee under bending from 0° to 90°. d) Corresponding optical and infrared (IR) images for an activated patch on the knee at different bending angles from 0° to 90°. All scale bars are 3.5 and 4 cm (insets). e) Change of resistance as function of temperature for a Cu NW-based sensing element. The slope denotes a sensitivity of the sensor (≈0.7 Ω °C^{-1}). f) Results of temperature mapping obtained from a 1 × 3 array device by placing preheated objects onto the left (black line) and right (blue line) areas of the device. g) A corresponding IR image during the measurements in (f). Scale bar is 1 mm.

and a control thin film-embedded elastomer, all mounted onto the knee under bending (θ = 0°–90°). Here, the elevated temperature aims to maintain constantly at 40–42 °C by modulating the incident powers (0.1–0.8 W) for which the final temperature remains below the maximum allowable temperature (≈45 °C) in human tissues to prevent any possible damages.[47] The results also show that the NW mesh-based thermal actuators maintain the elevated temperature under the complete bending angle (θ) up to ≈90°, whereas the thin film-based devices fail at θ = ≈60°, typically due to plastic deformations or catastrophic cracks. Figure 4d shows corresponding optical images and IR images (insets) of the activated device by incident power of 0.15 W. These results illuminate its potential utility in reliable means to provide therapeutic heat through the mechanically compliant contacts onto the joints without significant constraints on the natural movements.

The similar design principles can be extended to build a temperature sensor by exploiting the predictable change in resistance of the Cu NWs that follows by the change of environmental temperature.[48] Figure 4e shows a characterization curve for a representative Cu NW-based sensor without applying mechanical strains where the slope indicates the sensitivity (≈0.7 Ω °C^{-1}). Arrangement of multiple heating elements allows forming array types of sensors for mapping temperature in a spatial manner. Figure 4f presents results of the temperature mapping obtained from a 1 × 3 array sensor on an artificial skin by applying preheated (110 °C for ≈10 min) pieces of glass selectively onto left and right sides of the device in the room temperature environment. The temperature on the left (black line) and right areas (blue line) reaches 70–80 °C within ≈5 s upon heating whereas the temperature on the middle area (red line) remains below ≈40 °C. These results match well with the observations by exploiting an IR

Adv. Mater. 2016,
DOI: 10.1002/adma.201603878

camera (Figure 4g) where the highlighted areas (black and blue dotted boxes) indicate the pre-heated locations during the tests. The change of resistance would be affected by mechanical strains from the natural motions of wearers, and therefore simultaneous monitoring of strain and temperature would be necessary to compensate the correlation.

As another application example, **Figure 5**a,b presents schematic illustration and optical image of a skin-like electrophysiological monitor. The testbed device includes a thin layer of Cu NW mesh (1.0 g m^{-2}) and D-PI (300 nm thick) in the form of filamentary serpentine traces. The NW mesh-based electrodes that consist of reference, ground, and measurement configurations (from the left) are directly coupled to the skin. This arrangement allows high-quality recordings of electrocardiograms (ECG) and electromyograms (EMG) by applying the device on the chest (Figure 5c) and the forearm (Figure 5e) of a volunteer (age 28). The resulting ECG (Figure 5d) and EMG (Figure 5f) data by exploiting the Cu NW mesh-based electrodes (red color) are qualitatively comparable to those recorded with the control Cu thin film-based electrodes (blue color). Consistent with the abovementioned results, the Cu NW mesh-based electrodes exhibit excellent stretchability up to $\varepsilon \approx 80\%$ before fracture while the control Cu thin-film based electrodes fail typically at $\varepsilon \approx 40\%$–50% (Figure S12, Supporting Information). Representative optical images of the damaged Cu NW mesh-based electrodes upon stretching beyond the fracture limit (>80%) appear in Figure S13 (Supporting Information), highlighting the fracture points for this particular design of electrodes.

The novel design concept by combining highly networked NWs with an ultrathin elastomer offers a simple mean to enhance the important mechanical properties for broad ranges of skin-electronics, allowing the formation of robust contacts onto the epidermis under dynamic motions. This strategy raises the mechanical and electrical reliability of such systems against potential fracture and delamination by improving the overall crack resistance, contact adhesion, and normal/shear strength. Experimental and simulation results reveal the underlying mechanisms of the observed behaviors and provide opportunities to achieve a range of skin-coupled electronic systems. These strategies are applicable to other classes of stretchable electronics by providing solutions for improving mechanical durability against harsh loading conditions such as

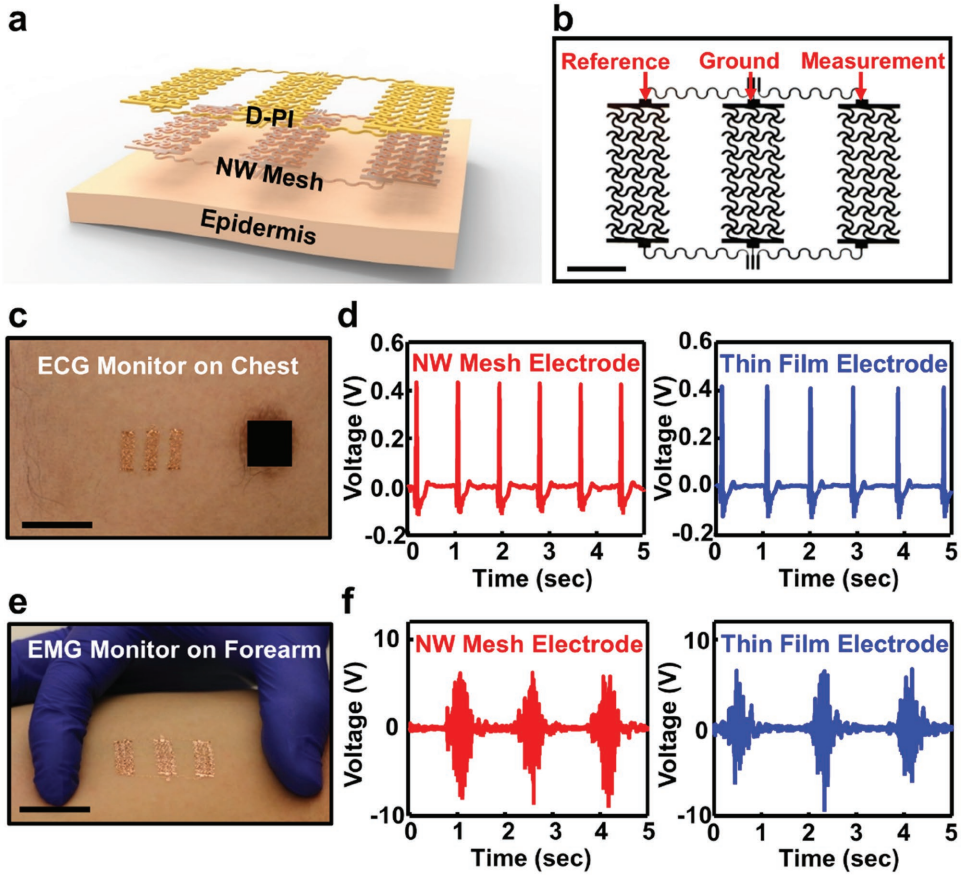

Figure 5. Device demonstrations in skin-like electrophysiological monitors. a) Exploded view schematic illustration of a skin-like electrophysiological monitor that contains a layer of Cu NW mesh. b) Optical image of a device with configuration of reference, measurement, and ground electrodes (from the left). Scale bar is 5 mm. c) Optical image of a device mounted on the chest for measurement of electrocardiogram (ECG). d) Results of ECG recording obtained from Cu NW mesh-based electrodes (left) and Cu thin film-based electrodes (right). e) Optical image of a device mounted on the forearm for measurement of electromyogram (EMG). f) Results of EMG recording obtained from Cu NW mesh-based electrodes (left) and Cu thin film-based electrodes (right), while clenching the first every 2 s. All scale bars are 2 cm.

over-stretching, scratching, and peeling by the users, or abrupt changes in temperature.

Experimental Section

Finite Element Analysis: The networked Cu NWs were modeled by a representative unit as shown in Figure S5 (left) (Supporting Information). The four networked Cu NWs (Young' modulus of 119 GPa, Poisson's ratio of 0.33) were formed in a rectangular shape to account for the random orientations.[37] The NWs were bonded to an elastomer substrate (Young's modulus of 60 kPa, Poisson's ratio of 0.49) that was modeled as a Neo-Hookean hyperelastic solid. A typical coefficient of friction of 0.29 was adopted to simulate friction between the NWs.[49] The FEA model showed that the maximum strain in the NWs reached the fracture limit of 3.0% when the networked NWs were stretched by 30%,[45] implying that the networked NWs can sustain local strain up to 30%. This criterion was then applied to a full model in the studies where the NW mesh-embedded traces were modeled as a continuum film for which fracture occurred when the local strain reached at 30%.

Fabrication of Cu NW Mesh: A conventional solution-based nucleation and growth mechanism was used for the synthesis of Cu NWs.[50,51] A mixture of sodium hydroxide (NaOH) powders (45 g, Sigma Aldrich) and copper nitrate ($Cu(NO_3)_2$) solution (0.05 g, Sigma Aldrich) was dissolved in 80 mL of deionized water with vigorous stirring. Aqueous solutions of ethylenediamine (EDA, 0.5 mL, Sigma Aldrich) and hydrazine (100 mL, 35 wt% in H_2O, Sigma Aldrich) were added in the solution to chemically functionalize the surface and prevent oxidation of Cu NWs, respectively. The chemical reaction changed color of the solution from blue to transparent within ≈5 min. Heating the mixture solution at 60 °C for 1 h, without stirring, lifted reddish layer of Cu NWs on the surface of the solution. Repeated centrifuges (Eppendorf, 5417R, ≈5 times) at 2000 rpm for 5 min separated the Cu NWs from remaining slurry. The refined Cu NWs were mixed with 20 mL of isopropanol (99.5%, Sigma Aldrich) in a glass vial, and then filtered through a Teflon filter (SterliTech, 0.2 µm pore size) by exploiting a vacuum pump (KODIVAC GHP-240, ≈10^4 Torr). Complete drying at room temperature for ≈5 min formed a thin layer of Cu NW mesh on the surface of the Teflon filter. The resulting single Cu NW exhibited ≈40–50 µm in length and 80–120 nm in diameter with aspect ratio of >≈400. The upside down Teflon filter was firmly pressed onto a receiver substrate to transfer the Cu NW mesh. Gentle removal of the Teflon filter completed the entire process.

Fabrication of Ag NW Mesh: A conventional solution-based multistep growth mechanism was used for the synthesis of Ag NWs.[52] The synthesis began with preheating of 50 mL of ethylene glycol (EG, J.T. Baker, 9300-03) in an oil bath (Chemglass Inc., CG-1100) at ≈150 °C for 1 h. 400 µL of copper (II) chloride ($CuCl_2$, 4×10^{-3} M, Sigma-Aldrich, 487847) and 15 mL of polyvinylpyrrolidone (PVP, 0.147 M, Sigma-Aldrich, 856568) were added in the preheated EG at an interval of 15 min. Injection of silver nitrate ($AgNO_3$, 15 mL, 0.094 M, Sigma-Aldrich, 10220) at a rate of 1 mL min^{-1} by exploiting a syringe pump (World Precision Instruments, AL-4000) changed the color of the aqueous solution from ivory to gray. Successive growth steps by repeating these procedures increased the length of Ag NWs up to ≈250 µm in maximum. All other fabrication procedures to form a mesh structure were similar to those described for the Cu NW mesh.

Fabrication of Cu Thin Film-Based Devices: The fabrication began with depositing Ni (≈300 nm thick) and casting D-PI (≈300 nm thick) layer onto a Si wafer by using electron-beam evaporator and spin-coater, respectively. A layer of the Cu thin film (≈600 nm thick) was deposited by using sputtering. Photolithographic patterning by exploiting photoresist (Clariant AZ5214, 3000 rpm, 30 s) with 365 nm optical lithography and wet etching with Cu etchant (Transene) defined open mesh serpentine layouts as a stretchable design. A schematic illustration of a representative system layout appears in Figure S14 (Supporting Information), showing the geometric details. Additional casting of a layer of poly(methyl methacrylate) (PMMA, ≈800 nm thick) on the top was formed to serve as a temporary protection layer from the environments. Immersion of the entire structure in water at room temperature followed by gentle mechanical peel-off with a temporary holder such as thermal release tape (Nitto Denko, Inc.) separated the stacked layers (Ni/D-PI/Cu thin film/PMMA/thermal release tape) from the Si wafer. The delaminated Ni layer on the bottom was eliminated by immersing in iron chloride ($FeCl_3$) for ≈30 s. Heating at 100 °C for ≈1 min removed the adhesion of the thermal release tape to release the remaining layers. Immersion in acetone eliminated the PMMA layer. The completed structure was then transferred onto water, allowing its retrieval onto target surfaces of interest.

Fabrication of NW Mesh-Based Devices: The fabrication began with depositing Ni (≈300 nm thick) and casting D-PI (≈300 nm thick) layer onto a Si wafer by using electron-beam evaporator and spin-coater, respectively. A layer of the as-prepared NW mesh was transferred on the top by using the methods as described above. Photolithographic patterning and wet etching through the layers defined open mesh layouts as a stretchable design. All other fabrication procedures were similar to those described for the Cu thin film-based devices above.

Fabrication of Artificial Synthetic Skin: Commercially available biocompatible silicone-based elastomers such as Dragon Skin (Dragon Skin 30, Smooth-On, Inc.) and Ecoflex (Ecoflex 30, Smooth-On) were used to fabricate an artificial skin. The Dragon Skin (1:1 ratio of part A and B by weight) was mixed with flesh tone silicone pigment (Slic Pig, Smooth-On, Inc., 3% by weight) to modulate the color. Degassing in a vacuum desiccator for ≈15 min eliminated the entrapped air. Pouring the prepared mixtures onto the forearm of a volunteer followed by curing for 1 h at room temperature defined the human skin-like textures onto the surface to serve as a mold. The fully cured layer was carefully peeled off and placed in a clean petri dish with textured surface up in the air. Another casting and peel-off of 1:1 ratio (part A and B by weight) of Ecoflex onto the mold completed the entire process.

Electrical Measurements of Electrophysiological Monitors: The electrodes configured with measurement, reference, and ground were connected with an anisotropic conductive cable (ACF; Elform, USA) to an external preamplifier and data acquisition system. Applying the electrodes onto the skin of chest and forearm of a volunteer (age 27) facilitated the capture of ECG and EMG signals, respectively. An instrument amplifier (AD620, Analog Devices, USA) amplified the voltage difference across the measurement and reference electrodes to reduce the common mode noise. The driven ground circuitry returned an inverted common mode noise as a feedback to the skin. A series of hardware analog amplifiers, active filters (low-pass, high-pass, and notch filter) refined the signal to enhance the signal-to-noise ratio. The amplifications were 60 and 80 dB with the passband of 0.5–100 and 10–400 Hz for the ECG and EMG, respectively. A data acquisition system (NI-USB 6361, National Instruments, USA) captured the conditioned signals at a sampling rate of 1 kHz, followed by additional data processing by exploiting LabVIEW software.

Supporting Information

Supporting Information is available from the Wiley Online Library or from the author.

Acknowledgements

S.H. and M.K.K. contributed equally to this work. C.H.L. gratefully acknowledges the startup supports from Purdue University of the Weldon School of Biomedical Engineering and the School of Mechanical Engineering. C.H.L. also acknowledges the funding from the Printing SMART Film Initiative and the Eli Lilly and Company (No. 209301). S.W. gratefully acknowledges the support from the ASME Applied Mechanics Division-Haythornthwaite Foundation Research Initiation Grant, and

DOI: 10.1002/adma.201603878

partial support from the National Science Foundation of China (Nos. 11272260, 11172022, 11572022, 51075327, and 11302038).

Received: July 21, 2016
Revised: September 2, 2016
Published online:

[1] D. H. Kim, J. Xiao, J. Song, Y. Huang, J. A. Rogers, *Adv. Mater.* **2010**, *22*, 2108.
[2] J. A. Rogers, *MRS Bull.* **2014**, *39*, 549.
[3] D. H. Kim, N. Lu, R. Ma, Y. S. Kim, R. H. Kim, S. Wang, J. Wu, S. M. Won, H. Tao, A. Islam, K. J. Yu, T. I. Kim, R. Chowdhury, M. Ying, L. Xu, M. Li, H. J. Chung, H. Keum, M. McCormick, P. Liu, Y. W. Zhang, F. G. Omenetto, Y. Huang, T. Coleman, J. A. Rogers, *Science* **2011**, *333*, 838.
[4] N. Matsuhisa, M. Kaltenbrunner, T. Yokota, H. Jinno, K. Kuribara, T. Sekitani, T. Someya, *Nat. Commun.* **2015**, *6*, 7461.
[5] S. Choi, H. Lee, R. Ghaffari, T. Hyeon, D. H. Kim, *Adv. Mater.* **2016**, *28*, 4203.
[6] W. Gao, S. Emaminejad, H. Y. Nyein, S. Challa, K. Chen, A. Peck, H. M. Fahad, H. Ota, H. Shiraki, D. Kiriya, D. H. Lien, G. A. Brooks, R. W. Davis, A. Javey, *Nature* **2016**, *529*, 509.
[7] C. Pang, J. H. Koo, A. Nguyen, J. M. Caves, M. G. Kim, A. Chortos, K. Kim, P. J. Wang, J. B. Tok, Z. Bao, *Adv. Mater.* **2015**, *27*, 634.
[8] J. A. Rogers, *JAMA* **2015**, *313*, 561.
[9] T. Someya, *Stretchable Electron.* **2013**, 143.
[10] T. Yokota, P. Zalar, M. Kaltenbrunner, H. Jinno, N. Matsuhisa, H. Kitanosako, Y. Tachibana, W. Yukita, M. Koizumi, T. Someya, *Sci. Adv.* **2016**, *2*, e1501856.
[11] S. Lee, A. Reuveny, J. Reeder, H. Jin, Q. Liu, T. Yokota, T. Sekitani, T. Isoyama, Y. Abe, Z. Suo, T. Someya, *Nat. Nanotechnol.* **2016**, *11*, 472.
[12] T. Yokota, Y. Inoue, Y. Terakawa, J. Reeder, M. Kaltenbrunner, T. Ware, K. Yang, K. Mabuchi, T. Murakawa, M. Sekino, W. Voit, T. Sekitani, T. Someya, *Proc. Natl. Acad. Sci. USA* **2015**, *112*, 14533.
[13] H. Lee, T. K. Choi, Y. B. Lee, H. R. Cho, R. Ghaffari, L. Wang, H. J. Choi, T. D. Chung, N. Lu, T. Hyeon, S. H. Choi, D. H. Kim, *Nat. Nanotechnol.* **2016**, *11*, 566.
[14] H. H. Chou, A. Nguyen, A. Chortos, J. W. To, C. Lu, J. Mei, T. Kurosawa, W. G. Bae, J. B. Tok, Z. Bao, *Nat. Commun.* **2015**, *6*, 8011.
[15] J. A. Fan, W. H. Yeo, Y. Su, Y. Hattori, W. Lee, S. Y. Jung, Y. Zhang, Z. Liu, H. Cheng, L. Falgout, M. Bajema, T. Coleman, D. Gregoire, R. J. Larsen, Y. Huang, J. A. Rogers, *Nat. Commun.* **2014**, *5*, 3266.
[16] R. C. Webb, A. P. Bonifas, A. Behnaz, Y. Zhang, K. J. Yu, H. Cheng, M. Shi, Z. Bian, Z. Liu, Y. S. Kim, W. H. Yeo, J. S. Park, J. Song, Y. Li, Y. Huang, A. M. Gorbach, J. A. Rogers, *Nat. Mater.* **2013**, *12*, 938.
[17] M. Kaltenbrunner, T. Sekitani, J. Reeder, T. Yokota, K. Kuribara, T. Tokuhara, M. Drack, R. Schwodiauer, I. Graz, S. Bauer-Gogonea, S. Bauer, T. Someya, *Nature* **2013**, *499*, 458.
[18] K. I. Jang, H. U. Chung, S. Xu, C. H. Lee, H. Luan, J. Jeong, H. Cheng, G. T. Kim, S. Y. Han, J. W. Lee, J. Kim, M. Cho, F. Miao, Y. Yang, H. N. Jung, M. Flavin, H. Liu, G. W. Kong, K. J. Yu, S. I. Rhee, J. Chung, B. Kim, J. W. Kwak, M. H. Yun, J. Y. Kim, Y. M. Song, U. Paik, Y. Zhang, Y. Huang, J. A. Rogers, *Nat. Commun.* **2015**, *6*, 6566.
[19] B. Xu, J. A. Rogers, *Extreme Mech. Lett.* **2016**, *7*, 44.
[20] S. Xu, Z. Yan, K.-I. Jang, W. Huang, H. Fu, J. Kim, Z. Wei, M. Flavin, J. McCracken, R. Wang, *Science* **2015**, *347*, 154.
[21] C. H. Lee, Y. Ma, K. I. Jang, A. Banks, T. Pan, X. Feng, J. S. Kim, D. Kang, M. S. Raj, B. L. McGrane, *Adv. Funct. Mater.* **2015**, *25*, 3698.
[22] P. Lee, J. Lee, H. Lee, J. Yeo, S. Hong, K. H. Nam, D. Lee, S. S. Lee, S. H. Ko, *Adv. Mater.* **2012**, *24*, 3326.
[23] K. K. Kim, S. Hong, H. M. Cho, J. Lee, Y. D. Suh, J. Ham, S. H. Ko, *Nano Lett.* **2015**, *15*, 5240.
[24] Y. Won, A. Kim, W. Yang, S. Jeong, J. Moon, *NPG Asia Mater.* **2014**, *6*, e132.
[25] S. Ye, A. R. Rathmell, Z. Chen, I. E. Steward, B. J. Wiley, *Adv. Mater.* **2014**, *26*, 6670.
[26] H. Wu, D. Kong, Z. Ruan, P. C. Hsu, S. Wang, Z. Yu, T. J. Carney, L. Hu, Y. Cui, *Nat. Nanotehchnol.* **2013**, *8*, 421.
[27] Y. Lee, T. Kim, S. Y. Min, W. Xu, S. Jeong, H. Seo, T. Lee, *Adv. Mater.* **2014**, *26*, 8010.
[28] Y. Lee, S. Y. Min, T. S. Kim, S. H. Jeong, J. Y. Won, H. Kim, W. Xu, J. K. Jeong, T. W. Lee, *Adv. Mater.* **2016**, DOI:10.1002/adma.201602855.
[29] C. H. Lee, D. R. Kim, X. Zheng, *Nano Lett.* **2011**, *11*, 3435.
[30] C. H. Lee, D. R. Kim, I. S. Cho, N. William, Q. Wang, X. Zheng, *Sci. Rep.* **2012**, *2*, 1000.
[31] C. H. Lee, J. H. Kim, C. Zou, I. S. Cho, J. M. Weisse, W. Nemeth, Q. Wang, A. C. van Duin, T. S. Kim, X. Zheng, *Sci. Rep.* **2013**, *3*, 2917.
[32] W. H. Yeo, Y. S. Kim, J. Lee, A. Ameen, L. Shi, M. Li, S. Wang, R. Ma, S. H. Jin, Z. Kang, Y. Huang, J. A. Rogers, *Adv. Mater.* **2013**, *25*, 2773.
[33] J. Kim, G. A. Salvatore, H. Araki, A. M. Chiarelli, Z. Xie, A. Banks, X. Sheng, Y. Liu, J. W. Lee, K. I. Jang, S. Y. Heo, K. Cho, H. Luo, B. Zimmerman, J. Kim, L. Yan, X. Feng, S. Xu, M. Fabiani, G. Gratton, Y. Huang, U. Paik, J. A. Rogers, *Sci. Adv.* **2016**, *2*, e1600418.
[34] S. Xu, Y. Zhang, L. Jia, K. E. Mathewson, K. I. Jang, J. Kim, H. Fu, X. Huang, P. Chava, R. Wang, S. Bhole, L. Wang, Y. J. Na, Y. Guan, M. Flavin, Z. Han, Y. Huang, J. A. Rogers, *Science* **2014**, *344*, 6179.
[35] T. Proulx, *Dynamic Behavior of Materials, Volume 1: Proceedings of the 2010 Annual Conference on Experimental and Applied Mechanics*, Vol. *1*, Springer Science & Business Media, Berlin, Germany, **2011**.
[36] D. H. Kim, R. Ghaffari, N. Lu, S. Wang, S. P. Lee, H. Keum, R. D. Angelo, L. Klinker, Y. Su, C. Lu, Y. S. Kim, A. Ameen, Y. Lid, Y. Zhang, B. D. Graff, Y. Y. Hsu, Z. Liu, J. Ruskin, L. Xu, C. Lu, F. G. Omenetto, Y. Huang, M. Mansour, M. J. Slepian, J. A. Rogers, *Proc. Natl. Acad. Sci. USA* **2012**, *109*, 19910.
[37] Y. Zhang, S. Wang, X. Li, J. A. Fan, S. Xu, Y. M. Song, K. J. Choi, W. H. Yeo, W. Lee, S. N. Nazaar, B. Lu, L. Yin, K. C. Hwang, J. A. Rogers, Y. Huang, *Adv. Funct. Mater.* **2014**, *24*, 2028.
[38] C. F. Guo, Y. Chen, L. Tang, F. Wang, Z. Ren, *Nano Lett.* **2016**, *16*, 594.
[39] N. Lu, X. Wang, Z. Suo, J. Vlassak, *Appl. Phys. Lett.* **2007**, *91*, 221909.
[40] N. Lu, Z. Suo, J. J. Vlassak, *Acta Mater.* **2010**, *58*, 1679.
[41] I. Lee, J. Lee, S. H. Ko, T.-S. Kim, *Nanotechnology* **2013**, *24*, 415704.
[42] S. Yun, X. Niu, Z. Yu, W. Hu, P. Brochu, Q. Pei, *Adv. Mater.* **2012**, *24*, 1321.
[43] S. Hong, H. Lee, J. Lee, J. Kwon, S. Han, Y. D. Suh, H. Cho, G. Shin, J. Yeo, S. H. Ko, *Adv. Mater.* **2015**, *27*, 4744.
[44] S. Chen, Y.-C. Liao, *Phys. Chem. Chem. Phys.* **2014**, *16*, 19856.
[45] C. Peng, Y. Zhan, J. Lou, *Small* **2012**, *8*, 1889.
[46] J. Wu, J. Zng, A. R. Rathmell, X. Zhao, B. J. Wiley, *Nano Lett.* **2013**, *13*, 2381.
[47] C. H. Lee, H. Kim, D. V. Harburg, G. Park, Y. Ma, T. Pan, J. S. Kim, N. Y. Lee, B. H. Kim, K.-I. Jang, *NPG Asia Mater.* **2015**, *7*, e227.
[48] Q. Huang, C. M. Lilley, M. Bode, R. Divan, *J. Appl. Phys.* **2008**, *104*, 023709.
[49] H. C. Hsu, J. H. Chien, S. L. Fu, presented at *6th IMPACT Int. Conf.*, Taipei, Taiwan, Oct. **2011**.
[50] A. R. Rathmell, S. M. Bergin, Y. L. Hua, Z. Y. Li, B. J. Wiley, *Adv. Mater.* **2010**, *22*, 3558.
[51] S. Han, S. Hong, J. Ham, J. Yeo, J. Lee, B. Kang, P. Lee, J. Kwon, S. S. Lee, M. Y. Yang, S. H. Ko, *Adv. Mater.* **2014**, *26*, 5808.
[52] J. Lee, P. Lee, D. Lee, S. S. Lee, S. H. Ko, *Cryst. Growth Des.* **2012**, *12*, 5598.